

## Time- and space-resolved measurements of Ar( $1s_5$ ) metastable density in a microplasma using diode laser absorption spectroscopy

This article has been downloaded from IOPscience. Please scroll down to see the full text article.

2011 J. Phys. D: Appl. Phys. 44 145202

(<http://iopscience.iop.org/0022-3727/44/14/145202>)

View [the table of contents for this issue](#), or go to the [journal homepage](#) for more

Download details:

IP Address: 129.7.16.18

The article was downloaded on 25/06/2013 at 20:15

Please note that [terms and conditions apply](#).

# Time- and space-resolved measurements of Ar( $1s_5$ ) metastable density in a microplasma using diode laser absorption spectroscopy

Sergey G Belostotskiy<sup>1,3</sup>, Tola Ouk<sup>1</sup>, Vincent M Donnelly<sup>1</sup>,  
Demetre J Economou<sup>1</sup> and Nader Sadeghi<sup>2</sup>

<sup>1</sup> Plasma Processing Laboratory, Department of Chemical and Biomolecular Engineering, University of Houston, Houston, TX 77204-4004, USA

<sup>2</sup> Laboratoire de Spectrométrie Physique (UMR C5588), Université J. Fourier de Grenoble & CNRS, B P 87, F-38402 Saint-Martin d'Hères Cedex, France

E-mail: [vmdonnelly@uh.edu](mailto:vmdonnelly@uh.edu) and [economou@uh.edu](mailto:economou@uh.edu)

Received 16 December 2010, in final form 5 February 2011

Published 22 March 2011

Online at [stacks.iop.org/JPhysD/44/145202](http://stacks.iop.org/JPhysD/44/145202)

## Abstract

Time- and space-resolved measurements of Ar( $1s_5$ ) metastable (Ar\*) density were carried out in a pulsed dc argon microplasma discharge, using diode laser absorption spectroscopy. The temporal behaviour of metastable density after discharge turn off (in the afterglow) depended on their spatial location in the microplasma. In the early afterglow, the Ar\* density decayed monotonically with time in the region around the sheath edge, while in the bulk plasma the Ar\* density showed a maximum with time. This behaviour was attributed to electron-ion dissociative recombination. Later in the afterglow, the Ar\* decay was everywhere monotonic with time, mainly due to three-body collisional quenching by ground state argon atoms. The time evolution of the Ar\* density in the afterglow predicted by a kinetic model is in good agreement with the experimental measurements.

(Some figures in this article are in colour only in the electronic version)

## 1. Introduction

High pressure (hundreds of Torr) microdischarges have attracted much attention due to numerous applications in plasma display panels, excimer radiation sources, chemical and biological sensors, microreactors, materials treatment and modification, sterilization and plasma surgery [1–19].

Microdischarge diagnostics are important to better understand the physics of microdischarges and to optimize device performance. However, the application of conventional diagnostics (e.g. Langmuir probes) is complicated due to the small size (hundreds of micrometres), high operating pressure (hundreds of Torr) and high power density (ten to hundreds of kW cm<sup>-3</sup>) of microdischarges. In contrast, non-intrusive

optical diagnostics are convenient for characterization of microdischarges.

Previously [18], diode laser absorption spectroscopy (DLAS) was used to obtain spatially resolved measurements of Ar( $1s_5$ ) metastable density (Ar\*) in a parallel plate direct current (dc) argon microdischarge. It was found that neutral gas heating resulted in decreasing Ar\* density with increasing microdischarge current (i.e. power). This is in contrast to behaviour observed in low pressure (<100 s mTorr) plasmas, where the metastable density increases with input power. However, these measurements could not provide information about the mechanisms of metastable production and loss in high pressure microdischarges.

In this work time- and space-resolved measurements of Ar\* density were performed in a pulsed dc argon high pressure microdischarge. Probing the Ar\* density as a function of time

<sup>3</sup> Currently with *Applied Materials, Inc.*, 974 East Arques Ave, Sunnyvale, CA 94085, USA.

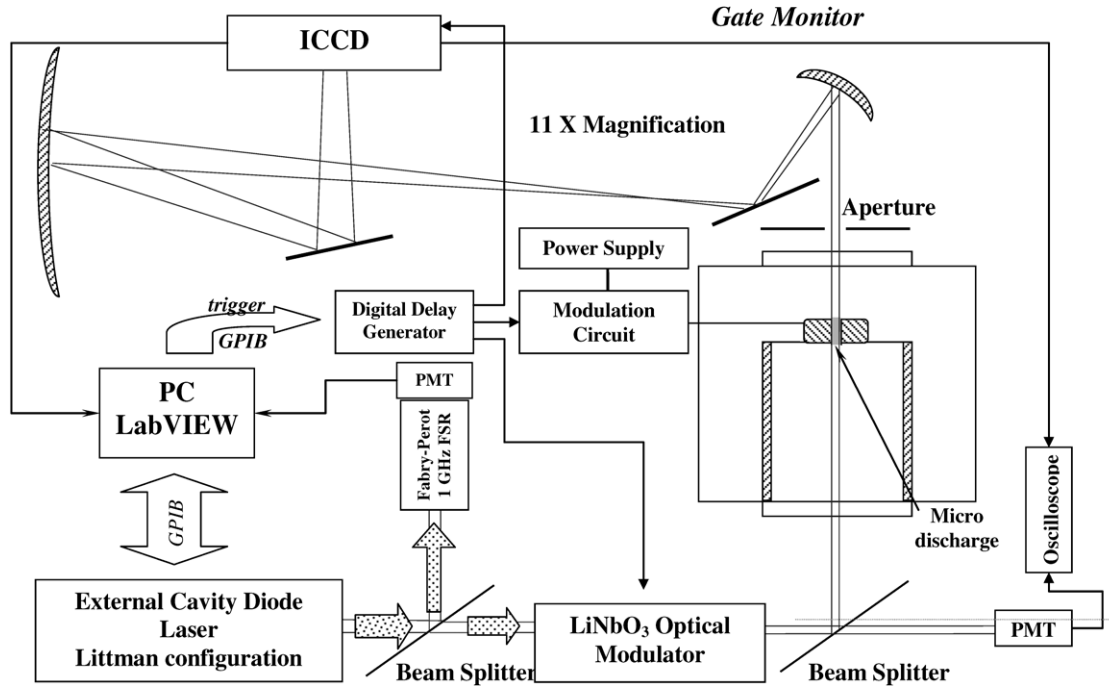


Figure 1. Experimental setup for time- and space-resolved DLAS.

in the afterglow (plasma power off) at different spatial locations in the microdischarge provided information about its formation and destruction kinetics.

**Experimental.** The experimental setup, shown in figure 1, was a modified version of the setup used by Belostotskiy *et al* [18]. A parallel plate slot-type microdischarge [12, 14], was sustained between two rectangular ( $5\text{ mm} \times 0.5\text{ mm}$ ) molybdenum electrodes, spaced  $300\ \mu\text{m}$  apart. An external cavity diode laser (ECDL) in the Littman configuration (LION—Sacher Lasertechnik, Marburg, Germany) was used as the light source. It was tuned to the  $\lambda = 801.48\text{ nm}$  argon line,  $\text{Ar}(2p_8) \leftarrow \text{Ar}(1s_5, ^3P_2)$  transition. The absorption spectral profile was recorded by scanning the laser frequency across the absorption line. The laser frequency was scanned by changing the voltage on the piezoelectric element that moved one of the cavity mirrors. The laser beam from the ECDL passed through a beam splitter guiding part of the beam to a Fabry–Perot interferometer (1 GHz free spectral range) to perform *in situ* calibration of the laser frequency.

Unlike the original DLAS setup which used continuous wave laser radiation [18], this system employed an external electro-optical modulator (Lithium Niobate Intensity Modulator, EOSPACE Inc., Redmond, WA), so that Ar metastables were probed with short ( $\tau_1 = 200\text{ ns}$ ) laser pulses. Furthermore, an intensified CCD (ICCD, Princeton Instruments model PI-MAX) was used for laser light detection. The ICCD operated in a gated mode, with a gate width of  $\tau_{\text{ICCD}} = 300\text{ ns}$ , that was synchronized with the laser pulse. This arrangement allowed measurement of the absorption signal over a specified time window during the operation of the pulsed dc plasma.

After passing through the interelectrode space, the laser beam was directed through an aperture to suppress emission

from the plasma by reducing the solid angle of light collection. A set of flat and concave mirrors magnified ( $11\times$ ) and imaged the laser light, through a red optical filter (2-64 Corning Glass filter), onto the photocathode of the ICCD camera. Pixel binning was applied in the direction parallel to the electrode surfaces to increase sensitivity and improve the signal-to-noise ratio. Each resulting macropixel corresponded to a certain position across the interelectrode gap, and spatially resolved measurements were obtained in a single acquisition.

The argon dc microdischarge was operated in a pulsed power mode. The laser probe was synchronized with the plasma pulse using a Delay Generator (DG 535, Stanford Research Systems Inc., Sunnyvale, CA), which was externally triggered by a personal computer (PC). Time-resolved measurements were performed by sweeping the plasma pulse with respect to the probing laser pulse. The experiment was controlled by LabVIEW (National Instruments, Austin, TX) from the PC via a GPIB interface and a National Instruments data acquisition board (NI PCI-6064E). To obtain the space-dependent Ar( $1s_5$ ) metastable densities at a given delay time, the Beer–Lambert law was applied to the recorded transmitted laser signals on the ICCD camera with and without the presence of microdischarge (see [18] for more detail).

## 2. Results and discussion

Profiles of Ar\* density across the microdischarge as a function of time after the discharge was turned off (i.e. in the afterglow) are shown in figure 2 for a discharge pressure of  $P = 100\text{ Torr}$  and current of  $I = 5\text{ mA}$ . The metastable density near the sheath edge (*sheath edge density*) and that in the bulk plasma (*bulk density*) show different temporal behaviour. The sheath edge density decays in the first  $\sim 2\ \mu\text{s}$ , while the bulk density

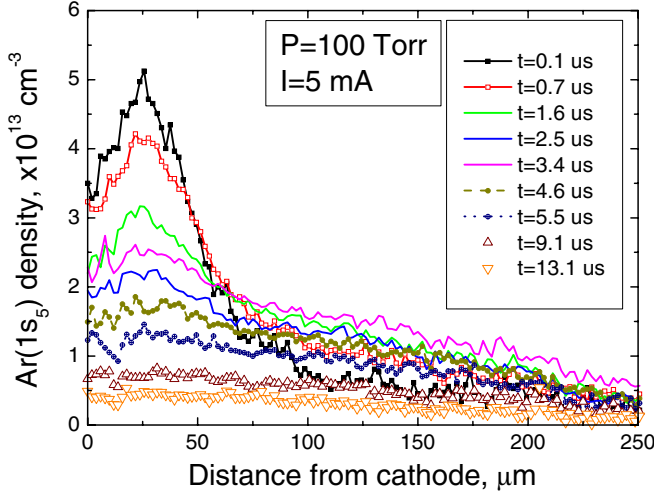


**Figure 2.** Spatially resolved  $\text{Ar}(1s_5)$  density profiles for different times in the afterglow.

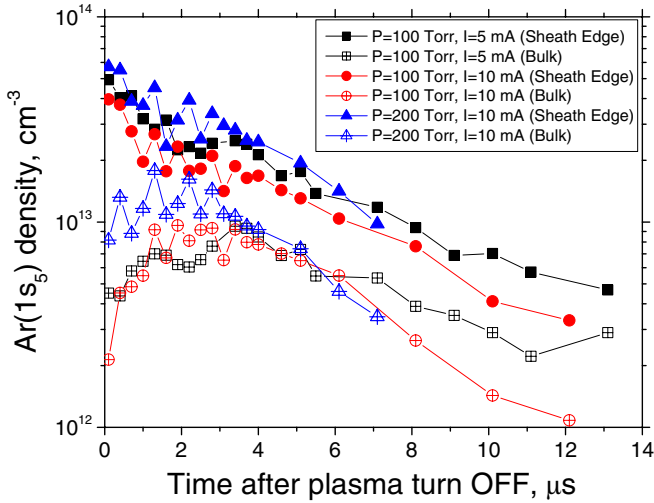
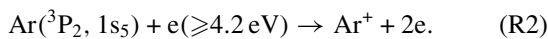
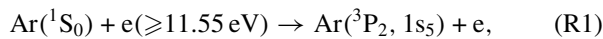


**Figure 3.** Time evolution of  $\text{Ar}^*$  density at the sheath edge and in the bulk plasma in the afterglow.

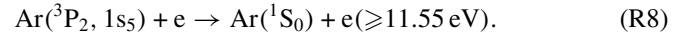
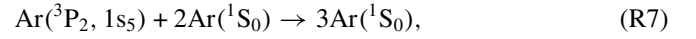
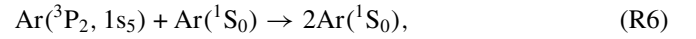
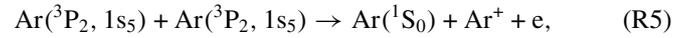
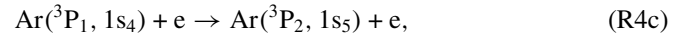
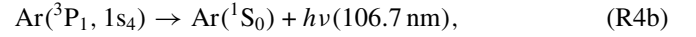
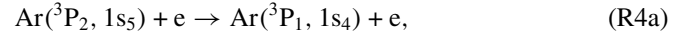
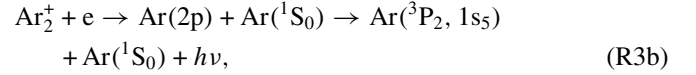
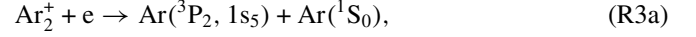
increases during this early afterglow time. Later in the afterglow, both the sheath edge and bulk metastable densities decay at a similar rate. The time evolution of the sheath edge ( $\sim 25 \mu\text{m}$  from the cathode) and bulk ( $\sim 210 \mu\text{m}$  from the cathode) metastable densities are shown in figure 3.

The observed spatiotemporal behaviour of  $\text{Ar}^*$  density can be understood by considering the production and loss mechanisms of argon metastables. At steady state,  $\text{Ar}^*$  production and loss are determined mainly by electron impact excitation and electron impact (stepwise) ionization, respectively [18]:



In the afterglow, the electron temperature decays rapidly ( $\sim 100 \text{ ns}$ ), resulting in drastic decrease in the rates of high threshold energy reactions such as (R1) and (R2). Under these conditions, other production and loss mechanisms come into play, such as electron-ion dissociative recombination

((R3a), (R3b)), electron impact collisional transfer to the resonant  $\text{Ar}(^3P_1, 1s_4)$  state followed by radiative decay to the ground state (R4a), (R4b), the reverse of reaction (R4a) (R4c), metastable pooling (R5), collisional quenching by ground state atoms (R6) and (R7) and collisional quenching by electrons (R8):



The rate coefficient of dissociative recombination is given by  $k_3 = 9.1 \times 10^{-7} (T_g/T_e)^{0.61} \text{ cm}^3 \text{ s}^{-1}$  for  $T_e$  in the range 300–8500 K. Here,  $T_g$  (in K) is the gas temperature, assumed equal to the ion temperature [24]. According to Royal and Orel [20] the dissociative recombination reaction (R3) yields mainly an Ar atom in the ground state and an Ar atom in the 2p ( $\sim 25\%$ ) or 1s ( $\sim 75\%$ ) state.  $\text{Ar}(2p)$  may in turn radiatively decay to the  $\text{Ar}(1s_5)$  state. The overall yield of  $\text{Ar}(1s_5)$  is not known. A rough estimation based on the statistical weights of the 1s manifold suggests that the yield of  $\text{Ar}(1s_5)$  should be around  $5/(5 + 3 + 3 + 1) \approx 0.4$ . Thus, in the absence of experimental data, the overall yield was taken equal to 40%.

Reaction (R4a) has a very low threshold ( $\sim 0.075 \text{ eV}$ ) compared with electron temperatures prevailing in the active discharge, so its rate coefficient ( $k_{4a} = 2 \times 10^{-7} \text{ cm}^3 \text{ s}^{-1}$ ) is taken to be independent of electron temperature [21]. However, in the afterglow (when the electron temperature plummets) this threshold is no longer neglected. For this purpose, an Arrhenius type expression was assumed  $k_{4a} = 2 \times 10^{-7} \exp(-0.075/T_e) \text{ cm}^3 \text{ s}^{-1}$ . The rate coefficient of the reverse reaction was calculated using detailed balancing (taking into account the statistical weights of the levels) as  $k_{4c} = \frac{5}{3} 2 \times 10^{-7} = 3.3 \times 10^{-7} \text{ cm}^3 \text{ s}^{-1}$ .

The resonant state  $\text{Ar}(^3P_1, 1s_4)$  decays very fast to the ground state (Einstein's coefficient  $A_{\text{rg}} = 1.19 \times 10^8 \text{ s}^{-1}$  [22]). However, at high pressures, resonant radiation is re-absorbed by ground state atoms resulting in so-called *radiation trapping*. The *effective* loss rate of  $\text{Ar}(^3P_1, 1s_4)$  atoms through reaction (R4b) is characterized by an escape factor, estimated using Holstein's theory [23, 24]. For slab geometry and Lorentzian lineshape, the escape factor is given by

$$g = \frac{1.15}{\sqrt{\pi k_0 L}}, \quad (1)$$

where  $k_0$  is the absorption coefficient at the centre of the spectral profile and  $L$  is the interelectrode gap. Under the present conditions, the spectral line of the resonant radiation ( $\lambda = 106.7$  nm) is not necessarily a pure Lorentzian. In fact, the Doppler width (FWHM), for the typical conditions of  $P \sim 100$  Torr and  $T_g \sim 600$  K, is  $\sim 5$  times larger than the Lorentzian FWHM. Nevertheless, at high opacity ( $k_0 L \gg 1$ ), radiation mainly ‘escapes’ through the *wings* of the spectral distribution. Thus, the Lorentzian component of the spectral lineshape dominates the ‘escape’ of radiation, even though the bulk of the spectral line is still governed by Doppler broadening.

The absorption coefficient can be calculated from [24]

$$k_0 = \frac{\lambda_0^2}{2\pi} \cdot \frac{g_r}{g_g} A_{rg} \left( \frac{\gamma_\omega}{N} \right)^{-1}, \quad (2)$$

where  $\lambda_0 = 106.7$  nm is the central wavelength,  $g_r/g_g = 3$  is the statistical weight ratio and  $\gamma_\omega/N$  is the reduced width of the Lorentzian profile (in units of angular frequency), which is governed by resonant broadening. The reduced width is given by [25]

$$\frac{\gamma_\omega}{N} \approx 2\pi \frac{1.45}{8} \lambda_0 c f_{rg} r_e \quad (\text{in cm}^3 \text{ s}^{-1}), \quad (3)$$

where  $c$  is the speed of light in vacuum,  $f_{rg} = 0.066$  is the oscillator strength of the transition and  $r_e = e^2/m_e c^2 = 2.818 \times 10^{-13}$  cm is a classical electron radius. In the high pressure limit, when the Lorentzian component of the spectral line dominates the ‘escape’ of radiation, the escape factor is independent of pressure. For the Ar resonant transition  $\text{Ar}(^3\text{P}_1, 1s_4) \rightarrow \text{Ar}(^1\text{S}_0)$  the escape factor, calculated using equations (1)–(3), was found to be  $g = 3.8 \times 10^{-3}$ , resulting in a loss frequency of  $\text{Ar}(^3\text{P}_1, 1s_4)$  given by  $\nu_{rg} = g A_{rg} = 4.6 \times 10^5 \text{ s}^{-1}$ .

The rate coefficients for reactions (R5)–(R7) were taken from [26] ( $k_5 = 6.4 \times 10^{-10} \text{ cm}^3 \text{ s}^{-1}$ ,  $k_6 = 2.3 \times 10^{-15} \text{ cm}^3 \text{ s}^{-1}$  and  $k_7 = 1.4 \times 10^{-32} \text{ cm}^6 \text{ s}^{-1}$ ), and the rate coefficient for reaction (R8) was taken from [27] ( $k_8 = 1 \times 10^{-9} \text{ cm}^3 \text{ s}^{-1}$ ).

Analysis of the metastable density evolution in the argon afterglow was based on a kinetic model accounting for five species: electrons, atomic ions  $\text{Ar}^+$ , molecular ions  $\text{Ar}_2^+$  and atoms in metastable  $\text{Ar}(1s_5)$  and resonant  $\text{Ar}(1s_4)$  states. The electron temperature in the afterglow was assumed to be  $T_e \sim 0.1$  eV. The initial conditions for bulk electron density ( $2 \times 10^{13} \text{ cm}^{-3}$ ) and gas temperature (600 K) were taken from [19]. The initial ( $t = 0$ ) densities of  $\text{Ar}^+$  and  $\text{Ar}_2^+$  were calculated from the mass balance of  $\text{Ar}_2^+$  ions coupled to the electroneutrality constraint:

$$k_9 N^2 \text{Ar}^+ - (k_3)_{T_e^0} n_e^0 \text{Ar}_2^+ = \frac{d\text{Ar}_2^+}{dt} = 0, \quad (4)$$

$$\text{Ar}^+ + \text{Ar}_2^+ = n_e,$$

where  $(k_3)_{T_e^0}$  is  $k_3$  evaluated at the steady-state temperature  $T_e^0$ , and  $k_9 = 2.5 \times 10^{-31} \text{ cm}^6 \text{ s}^{-1}$  is the rate coefficient for the production of molecular ions by reaction (R9),

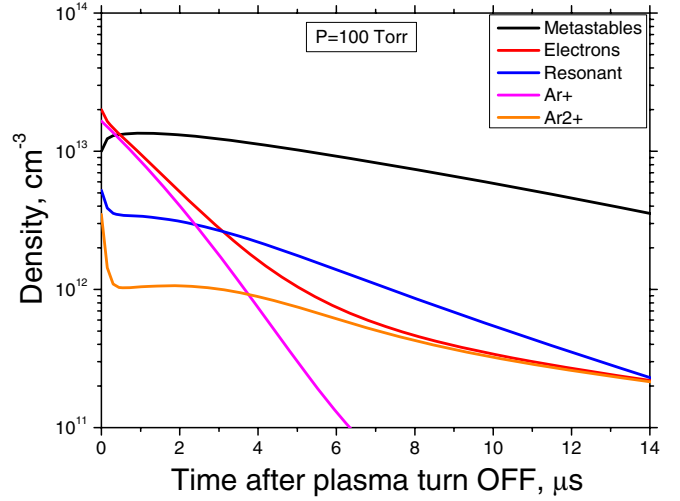
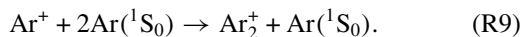


**Figure 4.** Time evolution of the densities of  $\text{Ar}(1s_5)$ , electrons,  $\text{Ar}(1s_4)$ ,  $\text{Ar}^+$  and  $\text{Ar}_2^+$  in the afterglow.

Solving the system of equations (4) one obtains the following expressions for the ion densities used as initial conditions for the afterglow calculation:

$$\text{Ar}^+ = n_e^0 \left( 1 - \frac{1}{1 + ((k_3)_{T_e^0} n_e^0 / k_9 N^2)} \right) \quad \text{at } t = 0, \quad (5)$$

$$\text{Ar}_2^+ = \frac{n_e^0}{1 + ((k_3)_{T_e^0} n_e^0 / k_9 N^2)} \quad \text{at } t = 0. \quad (6)$$

The bulk electron temperature in the steady-state microdischarge (before the voltage was turned off) was taken as  $T_e^0 \approx 1$  eV [14]. For a  $P = 100$  Torr,  $((k_3)_{T_e^0} n_e^0 / k_9 N^2) \approx 5$ , so  $\text{Ar}^+$  is the dominant ion ( $\sim 82\%$ ). The ratio  $\text{Ar}^+/\text{Ar}_2^+$  increases in the early afterglow, since the dissociative  $e\text{-Ar}_2^+$  recombination becomes faster as the electron temperature decreases. However, in the late afterglow, after the electron density has decayed enough ( $n_e < (k_9 N^2 / k_3)$ ),  $\text{Ar}_2^+$  takes over.

The initial density of resonant species  $\text{Ar}(1s_4)$  was found using the corresponding mass balance equation,

$$(k_{4a})_{T_e^0} n_e^0 \text{Ar}(1s_5) - k_{4c} n_e^0 \text{Ar}(1s_4) - g A_{rg} \text{Ar}(1s_4) = \frac{d\text{Ar}(1s_4)}{dt} = 0 \quad (7)$$

yielding

$$\text{Ar}(1s_4) = \text{Ar}(1s_5)^0 \frac{(k_{4a})_{T_e^0} n_e^0}{k_{4c} n_e^0 + g A_{rg}} \quad \text{at } t = 0. \quad (8)$$

The species densities as a function of time in the afterglow (calculated with the equations given above) are presented in figure 4. The rate of reactions involved in the  $\text{Ar}(1s_5)$  production and loss are presented in figure 5. The evolution of  $\text{Ar}(1s_5)$  density can be divided into two stages:

- (1) early afterglow (0 to a few  $\mu\text{s}$ ): the electron density is still high and electron reactions (including generation of metastables through the electron–ion recombination reaction (R3)) are important.

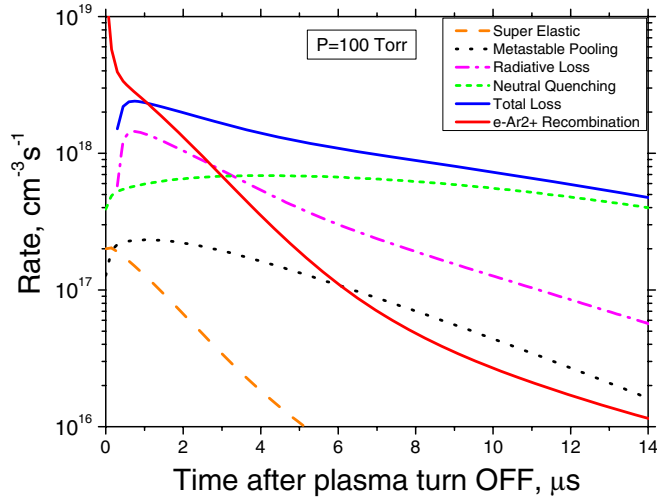


**Figure 5.** Rates of reactions involved in Ar( $1s_5$ ) production and loss during the afterglow.

(2) late afterglow (beyond a few  $\mu\text{s}$ ): the electron density has decayed to the point that electron reactions are unimportant and metastables are mainly quenched by three-body collisions (R7).

The early afterglow is defined by the following condition:

$$n_e \gg \frac{k_9 N^2}{k_3}. \quad (9)$$

For 100 Torr argon, this condition implies  $n_e \gg 10^{12} \text{ cm}^{-3}$ . Furthermore, for these levels of electron density, decay of electrons through  $e\text{-Ar}_2^+$  recombination (R3) is much faster than electron generation through metastable pooling reaction (R5). Making the pseudo steady-state (PSS) approximation for  $\text{Ar}_2^+$  (which is valid in view of equation (9)) yields

$$\text{Ar}_2^+ = \frac{n_e}{1 + (k_3 n_e / k_9 N^2)} \approx \frac{k_9 N^2}{k_3}, \quad (10)$$

where  $k_3$  is now evaluated at the afterglow  $T_e$ . One can then rewrite the electron balance equation as

$$\frac{dn_e}{dt} = -k_3 n_e \text{Ar}_2^+ \approx -k_9 N^2 n_e, \quad (11)$$

and solve for the electron density evolution,

$$n_e = n_e^0 \exp(-k_9 N^2 t). \quad (12)$$

The equation for metastable density can also be simplified. As seen in figure 5, in the early afterglow, one may neglect metastable pooling (R5), two-body collisional quenching by neutrals (R6) and quenching by electrons (R8). Then,

$$\frac{d\text{Ar}(1s_5)}{dt} = -k_7 N^2 \text{Ar}(1s_5) + 0.4 k_9 N^2 n_e - k_{4a} n_e \text{Ar}(1s_5) \left( 1 - \frac{k_{4c} \text{Ar}(1s_4)}{k_{4a} \text{Ar}(1s_5)} \right), \quad (13)$$

where  $k_{4a}$  is evaluated at the afterglow  $T_e$ . The factor of 0.4 multiplying  $k_9$  accounts for the 40% yield of reaction (R9) in producing metastables. In addition, if

$$n_e \gg \frac{g A_{\text{rg}}}{k_{4c}} \approx 10^{12} \text{ cm}^{-3}, \quad (14)$$

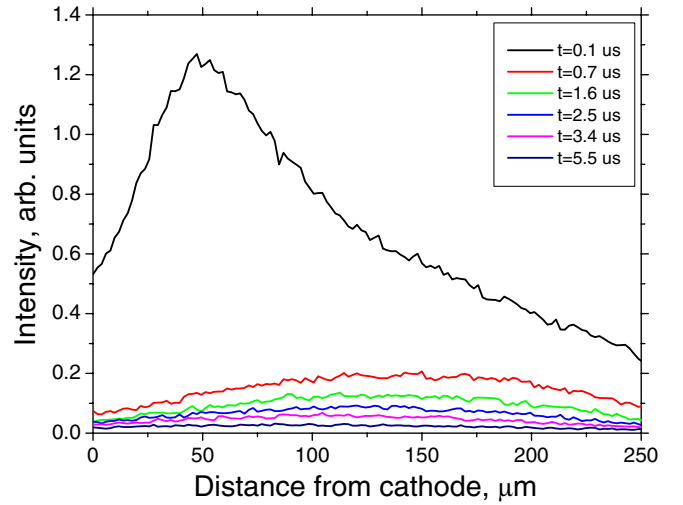


**Figure 6.** Plasma emission profiles for different times in the afterglow. Emission was filtered by a broadband optical filter, so that only the part of the spectrum with  $\lambda > 660 \text{ nm}$  was detected.

the radiative state is strongly coupled with the metastable state, and the PSS approximation can also be applied to  $\text{Ar}(1s_4)$ . Equation (14) is satisfied in the early afterglow in view of the condition imposed by equation (9). Applying the PSS approximation,

$$\text{Ar}(1s_4) = \text{Ar}(1s_5) \frac{k_{4a} n_e}{k_{4c} n_e + g A_{\text{rg}}} \quad (15)$$

and

$$\frac{d\text{Ar}(1s_5)}{dt} \approx -k_7 N^2 \text{Ar}(1s_5) + 0.4 \cdot k_9 N^2 n_e - \frac{k_{4a}}{k_{4c}} g A_{\text{rg}} \text{Ar}(1s_5). \quad (16)$$

Using the electron density equation (12), equation (16) can be solved analytically,

$$\text{Ar}(1s_5) = \text{Ar}(1s_5)^0 \exp(-\nu t) + \frac{0.4 \cdot k_9 N^2}{k_9 N^2 - \nu} n_e^0 (\exp(-\nu t) - \exp(-k_9 N^2 t)), \quad (17)$$

where  $\nu = (k_{4a}/k_{4c}) g A_{\text{rg}} + k_7 N^2$ . This equation provides the metastable density evolution in the early afterglow.

The characteristic time for the transition from the early afterglow to the late afterglow is found by combining equations (9) and (12)

$$n_e = \frac{k_9 N^2}{k_3} = n_e^0 \exp(-k_9 N^2 t_{\text{EL}}), \quad (18)$$

which gives  $t_{\text{EL}} \approx 4.7 \mu\text{s}$  at 100 Torr. In the late afterglow, the electron and ion densities have decayed to the point that reaction (R3) does not contribute to metastable production significantly, resulting in net metastable loss mainly through three-body collisional quenching by neutrals (R7).

Reaction (R3b) yields a photon in the  $\sim 800 \text{ nm}$  spectral range, giving rise to the emission in the near-IR, as observed in figure 6. In figure 6, the initial fast drop of emission intensity reflects the fast decay of electron temperature. After the initial drop, plasma emission decays with a characteristic time that

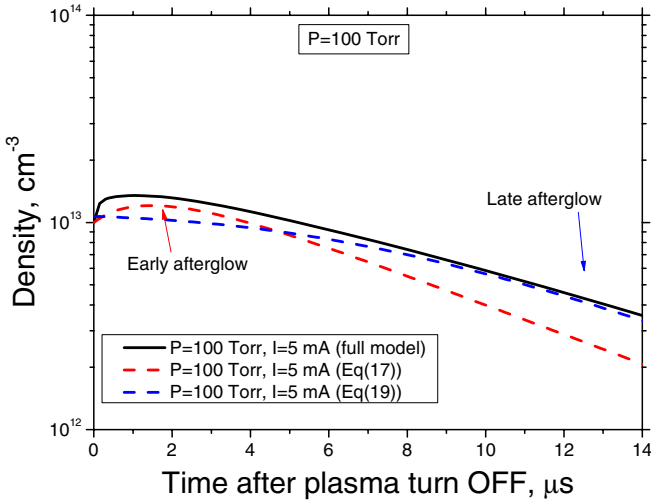


**Figure 7.** Comparison of the Ar ( $1s_5$ ) number density predictions of the full five-species kinetic model with the approximations given by equations (17) and (19).

corresponds to the metastable density decay timescale in the late afterglow ( $\sim 5 \mu\text{s}$ ). The spatial profile of plasma emission becomes nearly symmetric with respect to the central plane of the microdischarge, resembling a diffusion profile. Since diffusion of the radiating neutrals can be neglected under the conditions of the experiment (their diffusion length before radiating is  $\sqrt{D_n \tau_{\text{rad}}} < 10 \mu\text{m}$ ), the emission profile should reflect the spatial distribution of  $\text{Ar}_2^+$  density.

To describe the late afterglow one should consider gas cooling with a concomitant increase in gas density,  $N$ . For a 100 Torr afterglow, the characteristic heat conduction time is  $\tau_c = \Lambda^2/4\alpha \approx 7.5 \mu\text{s}$ , where  $\Lambda \sim 100 \mu\text{m}$  is the microplasma length scale and  $\alpha$  is the thermal diffusivity of the gas. For 100 Torr and 5–10 mA, the spatially averaged gas temperature decreased from  $\sim 600 \text{ K}$  in the steady-state microdischarge [19] to  $\sim 300 \text{ K}$  in the late afterglow. This corresponds to an increase in the rate of reaction (R7) from  $\sim 4 \times 10^4 \text{ s}^{-1}$  at 600 K to  $\sim 1.4 \times 10^5 \text{ s}^{-1}$  at 300 K. The experimental loss rate, extracted from the slope of  $\ln(\text{Ar}(1s_5))$  decay of figure 8, gives  $\nu_{\text{loss}} \approx 2.4 \times 10^5 \text{ s}^{-1}$ , consistent with the estimated value.

Therefore, in the late afterglow, the metastable density can be described by

$$\text{Ar}(1s_5) = \text{Ar}(1s_5)^* \exp\left(-k_7 \int_{t^*}^t N(z)^2 dz\right), \quad (19)$$

where  $t^*$  is the beginning of the late afterglow and  $\text{Ar}(1s_5)^*$  is the corresponding metastable density. Figure 7 shows a comparison of the metastable density calculated using the full five-species kinetic model with that predicted by the simplified model (equations (17) and (19)). The simplified model provides a reasonable account of the metastable density.

The time evolution of the spatially averaged  $\text{Ar}(1s_5)$  density measured experimentally is compared in figure 8 with the results of the full five-species kinetic model. The model captures the experimentally observed features in a quantitative manner. In the early afterglow, the average metastable density

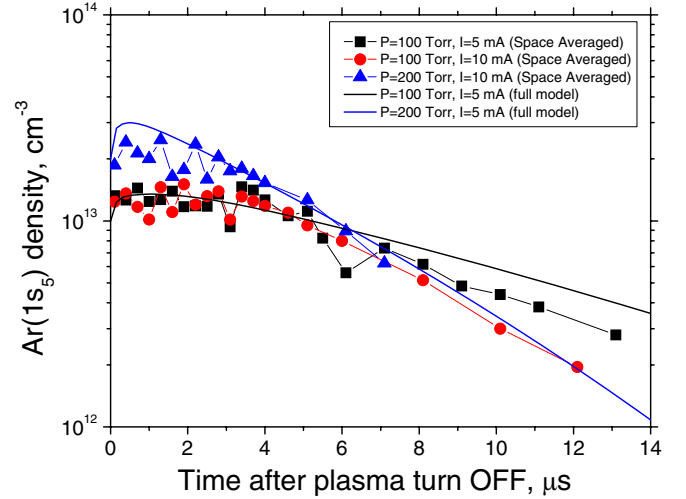


**Figure 8.** Time evolution of space-averaged metastable density in the afterglow: points—experimental results; solid lines—predictions of the full five-species kinetic model.

goes through a slight maximum because of the relatively high production rate through electron–ion recombination. Later in the afterglow, when the electron density has decayed sufficiently, the evolution of metastable density is governed by the three-body collisional quenching (R7).

### 3. Conclusions

Time- and space-resolved measurements of  $\text{Ar}(1s_5)$  metastable ( $\text{Ar}^*$ ) density were carried out in a pulsed argon dc microdischarge, using DLAS. The time evolution of  $\text{Ar}^*$  density in the afterglow (plasma off) depended on position in the microdischarge. Around the sheath edge, the  $\text{Ar}^*$  density decayed monotonically with time, while in the bulk plasma the  $\text{Ar}^*$  density went through a maximum in the early (0 to few  $\mu\text{s}$ ) afterglow.

This behaviour was attributed to dissociative recombination of  $\text{Ar}_2^+$  with electrons, yielding  $\text{Ar}^*$  as one of the products. In the bulk, during the early afterglow,  $\text{Ar}^*$  production by dissociative recombination exceeded  $\text{Ar}^*$  loss by pooling reactions, and by ground state atom and electron quenching. Thus, the  $\text{Ar}^*$  density exhibited a maximum with time. The opposite situation prevailed in the sheath edge region.

Later in the afterglow, the  $\text{Ar}^*$  decay was everywhere monotonic with time. During this period, the charge density was too low for dissociative recombination to be a significant source of metastables, and the  $\text{Ar}^*$  loss rate was dominated by three-body collisional quenching. Due to gas cooling in the afterglow, the neutral gas density in the microdischarge increased, causing an increase in the metastable loss rate.

A five-species kinetic model of the argon afterglow was developed. The time evolution of the  $\text{Ar}^*$  density predicted by the model was in good agreement with the experimental measurements. Approximate analytical expressions were also provided for the bulk  $\text{Ar}^*$  density as well as for the transition time from the early afterglow to the late afterglow.

## Acknowledgments

Financial support for this work was provided by the Department of Energy (DE-FG02-03ER54713), and the University of Houston GEAR program.

## References

- [1] Becker K H, Schoenbach K H and Eden J G 2006 Microplasmas and applications *J. Phys. D: Appl. Phys.* **39** R55–R70
- [2] Kushner M J 2005 Modelling of microdischarge devices: plasma and gas dynamics *J. Phys. D: Appl. Phys.* **38** 1633–43
- [3] Kogelschatz U 2004 Atmospheric-pressure plasma technology *Plasma Phys. Control. Fusion* **46** B63–B75
- [4] Boeuf J P 2003 Plasma display panels: physics, recent developments and key issues *J. Phys. D: Appl. Phys.* **36** R53–R79
- [5] Tachibana K, Kishimoto Y, Kawai S, Sakaguchi T and Sakai O 2005 Diagnostics of microdischarge-integrated plasma sources for display and materials processing *Plasma Phys. Control. Fusion* **47** A167–77
- [6] Hassaballa S, Yakushiji M, Kim Y K, Tomita K, Uchino K and Muraoka K 2004 Two-dimensional structure of PDP micro-discharge plasmas obtained using laser Thomson scattering *IEEE Trans. Plasma Sci.* **32** 127–34
- [7] Stoffels E, Flikweert A J, Stoffels W W and Kroesen G M W 2002 Plasma needle: a non-destructive atmospheric plasma source for fine surface treatment of (bio)materials *Plasma Sources Sci. Technol.* **11** 383–8
- [8] Hopwood J, Iza F, Coy S and Fenner D B 2005 A microfabricated atmospheric-pressure microplasma source operating in air *J. Phys. D: Appl. Phys.* **38** 1698–703
- [9] Wang Q, Koleva I, Donnelly V M and Economou D J 2005 Spatially resolved diagnostics of an atmospheric pressure direct current helium microplasma *J. Phys. D: Appl. Phys.* **38** 1690–7
- [10] Wang Q, Economou D J and Donnelly V M 2006 Simulation of a direct current microplasma discharge in helium at atmospheric pressure *J. Appl. Phys.* **100** 023301
- [11] Wang Q, Doll F, Donnelly V M, Economou D J, Sadeghi N and Franz G F 2007 Experimental and theoretical study of the effect of gas flow on gas temperature in an atmospheric pressure microplasma *J. Phys. D: Appl. Phys.* **40** 4202–11
- [12] Belostotskiy S G, Wang Q, Donnelly V M, Economou D J and Sadeghi N 2006 Three-dimensional gas temperature measurements in atmospheric pressure microdischarges using Raman scattering *Appl. Phys. Lett.* **89** 251503
- [13] Belostotskiy S G, Donnelly V M and Economou D J 2008 Influence of gas heating on high pressure dc microdischarge  $I$ - $V$  characteristics *Plasma Sources Sci. Technol.* **17** 045018
- [14] Belostotskiy S G, Khandelwal R, Wang Q, Donnelly V M, Economou D J and Sadeghi N 2008 Measurement of electron temperature and density in an argon microdischarge by laser Thomson scattering *Appl. Phys. Lett.* **92** 221507
- [15] Choi J, Iza F, Lee J K and Ryu C M 2007 Electron and ion kinetics in a DC microplasma at atmospheric pressure *IEEE Trans. Plasma Sci.* **35** 1274–8
- [16] Arkhipenko V I, Kirillov A A, Safronau Y A, Simonchik L V and Zgirouski S M 2008 Influence of cathode temperature on the parameters of an atmospheric pressure dc glow discharge *Plasma Sources Sci. Technol.* **17** 045017
- [17] Staack D, Farouk B, Gutsol A and Fridman A 2008 DC normal glow discharges in atmospheric pressure atomic and molecular gases *Plasma Sources Sci. Technol.* **17** 025013
- [18] Belostotskiy S G, Donnelly V M, Economou D J and Sadeghi N 2009 Spatially resolved measurements of argon metastable ( $1s_5$ ) density in a high pressure microdischarge using diode laser absorption spectroscopy *IEEE Trans. Plasma Sci.* **37** 852–8
- [19] Belostotskiy S G, Ouk T, Donnelly V M, Economou D J and Sadeghi N 2010 Gas temperature and electron density profiles in an argon dc microdischarge measured by optical emission spectroscopy *J. Appl. Phys.* **107** 053305
- [20] Royal J and Orel A E 2006 Dissociative recombination of  $\text{Ar}_2^+$  *Phys. Rev. A* **73** 042706
- [21] Ferreira C M, Loureiro J and Ricard A 1985 Populations in the metastable and the resonance levels of argon and stepwise ionization effects in a low-pressure argon positive-column *J. Appl. Phys.* **57** 82–90
- [22] 'NIST: Atomic Spectra Database,' <http://physics.nist.gov/PhysRefData/ASD/index.html>
- [23] Holstein T 1947 Imprisonment of resonant radiation in gases *Phys. Rev.* **72** 1212–33
- [24] Holstein T 1951 Imprisonment of resonance radiation in gases: II *Phys. Rev.* **83** 1159–68
- [25] Copley G H and Camm D M 1974 Pressure broadening and shift of argon emission lines *J. Quant. Spectrosc. Radiat. Transfer* **14** 899–907
- [26] Bogaerts A and Gijbels R 1995 Modeling of metastable argon atoms in a direct-current glow-discharge *Phys. Rev. A* **52** 3743–51
- [27] Donnelly V M 2004 Plasma electron temperatures and electron energy distributions measured by trace rare gases optical emission spectroscopy *J. Phys. D: Appl. Phys.* **37** R217